

1
2
3
4
5
6
7
8
9
10
11
12
13
14
15
16
17
18
19
20
21
22
23
24
25
26
27
28
29
30
31
32
33
34
35
36
37
38
39
40
41
42
43
44
45
46
47
48
49
50
51
52
53
54
55
56
57
58
59
60

Tuning shape, composition and magnetization of three-dimensional cobalt nanowires grown by Focused Electron Beam Induced Deposition (FEBID)

Javier Pablo-Navarro ¹, Dédalo Sanz-Hernández ², César Magén ^{1,3,4}, Amalio Fernández-Pacheco ²
and José María de Teresa ^{1,3,5,*}

¹ Laboratorio de Microscopías Avanzadas (LMA), Instituto de Nanociencia de Aragón (INA),
Universidad de Zaragoza, 50018 Zaragoza, Spain

² Cavendish Laboratory, University of Cambridge, JJ Thomson Cambridge, CB3 0HE, United Kingdom.

³ Departamento de Física de la Materia Condensada, Universidad de Zaragoza, 50009 Zaragoza, Spain

⁴ Fundación ARAID, Zaragoza, Spain

⁵ Instituto de Ciencia de Materiales de Aragón, Facultad de Ciencias, Universidad de Zaragoza – CSIC,
50009 Zaragoza, Spain

*Email: deteresa@unizar.es

Abstract

Electron beam induced deposition of three-dimensional cobalt nanowires with simultaneous high metallic content (≈ 80 % at.) and small diameter (< 100 nm) has been achieved by optimization of the growth parameters. Two different growth modes have been identified, denoted as *radial* and *linear*. In the *radial* mode, the wire diameter is at least ≈ 120 nm and the Co content is greater than ≈ 85 % at.. In the *linear* mode, the diameter is smaller than 80 nm and the Co content is at best

1
2
3 ≈80% at.. A sharp transition between both growth modes can occur inside a single nanowire for
4
5 certain experimental conditions. Electron holography measurements indicate that in optimized Co
6
7 nanowires the magnetic induction is high enough for applications in spintronics and magnetic
8
9 sensing and actuation at the nanoscale.
10
11

12
13
14
15
16
17 Keywords: cobalt nanowires, focused electron beam induced deposition, electron holography,
18
19 magnetic nanowires
20
21

22 23 24 25 **1. Introduction** 26

27
28 Thin-film layers and multilayers based on magnetic materials have nowadays various
29
30 applications in the fields of sensors and data storage, like in hard disks [1] [2]. On the other hand,
31
32 individual magnetic nanostructures are being investigated for their potential application in sensors
33
34 [3], memories [4] and logic [5]. Although most of the approaches for their fabrication rely on
35
36 standard lithography processes performed onto magnetic thin films and multilayers, a growing
37
38 interest exists on three-dimensional magnetic nanostructures, whose fabrication is challenging.
39
40 Focused Electron Beam Induced Deposition (FEBID) is one of the techniques that allow
41
42 addressing the growth of three-dimensional structures [6] [7] [8] [9] [10], in particular those based
43
44 on magnetic materials [11] [12] [13] [14] [15] [16] [17] [18] [19] [20]. In FEBID, precursor
45
46 molecules delivered by a Gas Injection System (GIS) close to the substrate become dissociated by
47
48 a focused electron beam, producing a deposit [21] [22] [23] [24]. The shape of the deposit is
49
50 determined by the electron beam scan as well as complex interactions between the electron beam,
51
52 substrate, precursor molecules and growing structure [25] [26]. The use of precursor molecules
53
54
55
56
57
58
59
60

1
2
3 containing magnetic elements such as Co, Fe and Ni permits the growth of magnetic deposits [11]
4 [27] [28] [29] [30] [31] [32] [33] and a large development has been made towards the growth of
5 magnetic deposits with high metal content, high magnetization, high resolution and complex
6 shapes, as recently reviewed [34] [35]. Such development has been focused on the optimization of
7 thin in-plane magnetic layers, whereas limited work has been done with regard to three-
8 dimensional magnetic deposits. However, there are many promising applications of three-
9 dimensional magnetic deposits in scanning probe techniques (such as Magnetic Force Microscopy
10 [17] and Ferromagnetic Resonance Force Microscopy [36]), racetrack-type magnetic memories
11 [14], Hall sensors [37] [38], nano-magnet logic [17] [39], superconducting vortex lattice pinning
12 [40], remote magneto-mechanical actuation [20], etc.

13
14
15
16
17
18
19
20
21
22
23
24
25
26
27
28 In the present work, we investigate in detail the interplay of the precursor flux and the electron
29 beam current in the physical properties of out-of-plane magnetic nanowires grown by FEBID using
30 the $\text{Co}_2(\text{CO})_8$ precursor. Our focus is put on the characterization of the obtained nanowire's
31 diameter, composition and magnetization, with the aim of growing narrow nanowires (< 100 nm
32 in diameter), with high Co content ($> 80\%$ at.) and magnetization approaching the bulk value
33 (1.8 T).
34
35
36
37
38
39
40
41
42

43 Previous work on the growth of three-dimensional nanowires by FEBID has shown the relevance
44 of several parameters that should be taken into account. For example, the use of sub-nA electron
45 beam currents produced by field-emission guns is suitable for the growth of narrow nanowires
46 (< 100 nm in diameter) [14] [41]. Additionally, the interaction of the primary electron beam with
47 the substrate and the growing structure also depends on the primary electron beam energy [42]
48 [43]. The balance between the availability of precursor molecules on the growth area and the
49 electron beam current is very important because it will determine whether the growth occurs in the
50
51
52
53
54
55
56
57
58
59
60

1
2
3 precursor-limited regime or the electron-limited regime, which will affect not only the growth rate
4 but also the composition of the nanowire [44]. However, this equilibrium can be strongly modified
5
6 when thermal heating of the growing deposit occurs, as previously found in FEBID [45] [46] [47]
7
8 [48]. On the one hand, an increase of temperature in the area of growth will change the precursor
9
10 residence time, affecting the growth rate and potentially the growth regime. On the other hand, the
11
12 decomposition of the precursor molecules will be faster if temperatures close to the thermal
13
14 decomposition of the precursor are reached. Moreover, thermal effects can be of tremendous
15
16 importance in three-dimensional nanostructures given that precursor replenishment in the area of
17
18 growth occurs at a lower rate compared to in-plane deposits because the diffusion mechanism of
19
20 precursor molecules from the substrate will be weakened as the deposit grows in height. In fact,
21
22 our results presented hereafter have identified a set of growth parameters that produce a change in
23
24 the diameter during the growth of a single nanowire. This is a consequence of the subtle balance
25
26 between the different factors governing the growth of three-dimensional nanowires, as discussed
27
28 hereafter.
29
30
31
32
33
34
35
36

37 **2. Experimental**

38 *2.1 Growth of the three-dimensional nanowires by FEBID*

39
40
41 The nanowires were grown in commercial Helios Nanolab 600 and 650 Dual Beam equipment
42
43 using the Schottky field-emission electron gun and a GIS that delivers the $\text{Co}_2(\text{CO})_8$ precursor.
44
45 The substrates were naturally-oxidized Si wafers. FEBID-Co deposits were grown with low
46
47 electron beam currents (< 100 pA). The working voltage was fixed to 5 kV given that initial
48
49 experiments did not lead to significant changes in the composition from 5 kV to 30 kV. The
50
51 nanowires were grown in spot mode, where the electron beam is continuously irradiating a single
52
53
54
55
56
57
58
59
60

1
2
3 point. A base pressure of 1×10^{-6} mbar existed in the working chamber before the injection of the
4
5 precursor. The $\text{Co}_2(\text{CO})_8$ precursor flux was tuned via a manual valve, which permits to vary the
6
7 chamber pressure during growth up to $\sim 4 \times 10^{-5}$ mbar. Given the linear relationship between the
8
9 chamber pressure increase during gas injection (ΔP) and the precursor flux (J), $J \propto \Delta P$ [49],
10
11 monitorization of the chamber pressure during growth allows us to establish relative correlations.
12
13
14

15 16 *2.2 Compositional analysis by Energy Dispersive X-ray Spectroscopy (EDS)*

17
18
19 Some of the EDS experiments were performed inside Helios Nanolab 650 Dual Beam equipment,
20
21 using an excitation electron beam voltage of 5 kV, beam current of 800 pA, and analyzed with the
22
23 EDAX software using APOLLO X detector. Other EDS experiments were carried out inside an
24
25 FEI Tecnai F30 Transmission Electron Microscopy (TEM) equipment operated at 300 kV. In this
26
27 case, the used software was Genesis RTEM, which is a tool embedded in FEI's TIA software
28
29 package, using a 136-5 detector from EDAX. The material composition was determined through
30
31 these experiments with a typical error of $\sim 2\%$ at. for main components assuming uniform
32
33 composition in the nanostructure. Along the manuscript, the composition is always expressed in
34
35 at. %.
36
37
38
39
40
41

42 *2.3 Compositional analysis by Energy Electron Loss Spectroscopy (EELS)*

43
44
45 EELS experiments were performed in an FEI Tecnai F30 equipment and in a probe-corrected
46
47 Titan Low Base 60-300 equipment, both operated at 300 kV. The first one is fitted with the Tridiem
48
49 863 Gatan Energy Filter (GIF) whereas the second one is equipped with a high brightness Schottky
50
51 electron gun (S-FEG), a CETCOR corrector for the condenser system to provide sub-Angstrom
52
53 probe size, and a Tridiem GIF (866 ERS). The spectroscopic experiments were carried out with a
54
55
56
57
58
59
60

1
2
3 25 mrad convergence semi-angle and EELS spectra were performed with an energy dispersion of
4
5 0.8 eV and energy resolution around 1.5 eV.
6
7

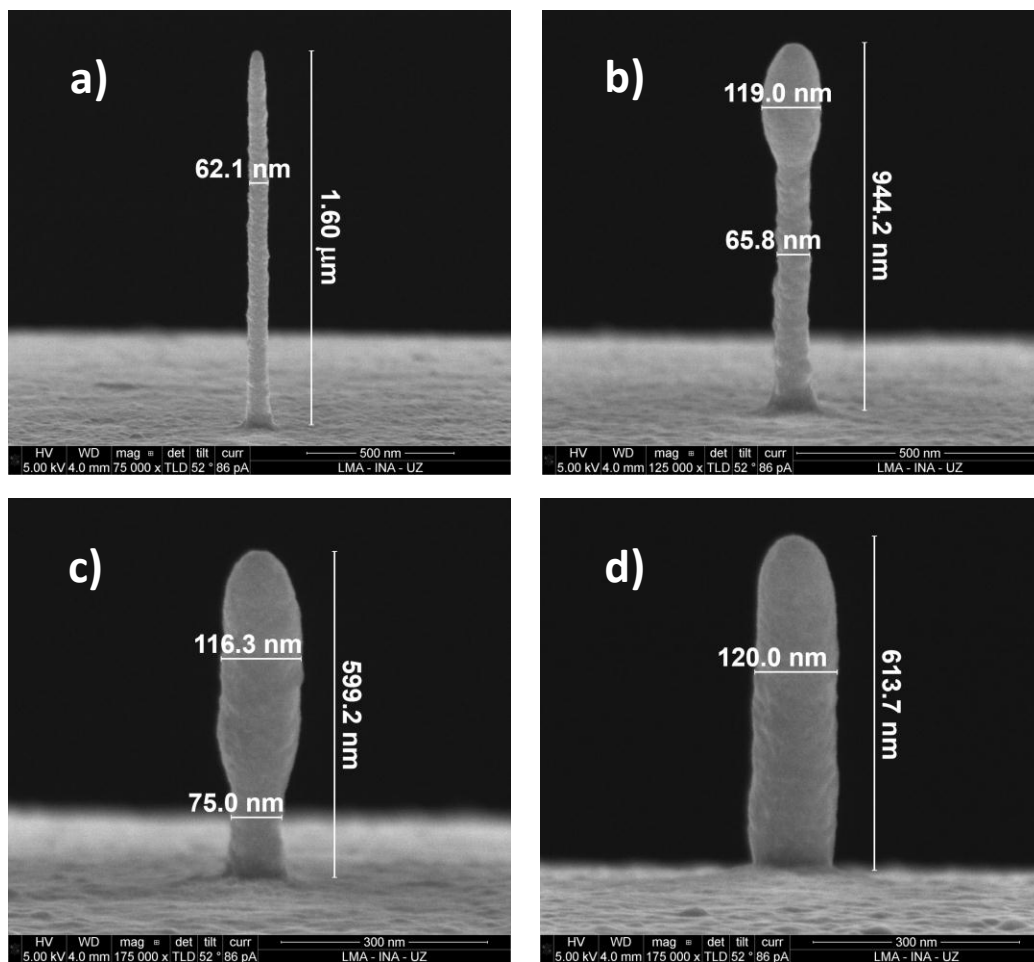
8 9 *2.4 Analysis of the magnetic induction by Electron Holography (EH) inside a Transmission* 10 11 *Electron Microscope (TEM)* 12

13
14 EH was carried out in an image-corrected FEI Titan Cube 60-300 TEM equipment operated at
15
16 300 kV and equipped with an S-FEG and a CETCOR corrector for the objective lens and a
17
18 motorized electrostatic biprism. The experiments were performed in Lorentz mode (with the
19
20 objective lens switched off, and the Lorentz lens, fitted below the objective lens, operating as the
21
22 image-forming lens). In the holographic experiments, the excitation of the biprism was varied
23
24 between 180 and 220 V, depending on the actual diameter of the NWs, to produce holograms with
25
26 a fringe contrast range of 20-25%. The acquisition time of the holograms was set to 5 s. The method
27
28 to extract the magnetic induction has been described in detail in a previous publication [41].
29
30
31
32

33 34 **3. Results** 35

36
37 As previously mentioned, a low electron beam current is a pre-requisite for the growth of small-
38
39 diameter nanowires. First, we present the results obtained using an electron beam current of 86 pA.
40
41 As can be observed in Figure 1(a), a narrow nanowire with diameter of 62 nm and an aspect ratio
42
43 of 25 is obtained when ΔP is 7.3×10^{-6} mbar. However, a decrease in ΔP to 6.4×10^{-6} mbar
44
45 provokes a change in the growth mode at the height of 650 nm, resulting in a nanowire with a
46
47 small diameter in the first segment (66 nm) and larger diameter in the second one (119 nm), as
48
49 shown in Figure 1(b). A further decrease in ΔP to 5.9×10^{-6} mbar induces the appearance of the
50
51 larger diameter closer to the substrate, at the height of 160 nm (see Figure 1(c)). If an even lower
52
53 ΔP of 5.1×10^{-6} mbar is used, the nanowire grows from the beginning in the mode with larger
54
55
56
57
58
59
60

1
2
3 diameter, 120 nm, as shown in Figure 1(d). Hereafter, the growth mode with smaller diameter is
4 referred as “linear regime” whereas the growth mode with larger diameter is referred as “radial
5 regime”. It is experimentally observed that if the growth current is increased, the radial-to-linear
6 crossover occurs at higher precursor flux (chamber growth pressure). A quantitative model to
7 explain this change in the mode of growth is beyond the scope of the present article given its
8 complexity, but is being currently addressed by the authors. Thermal and/or diffusion effects are
9 expected to play a crucial role in the observed effect. Thus, an increased thermal desorption of the
10 precursor [50] will occur due to an increased temperature at the tip of the nanowire due to reduced
11 thermal dissipation at long wire lengths. Additionally, a reduced number of molecules will be able
12 to diffuse from the substrate as the nanowire grows.



1
2
3 **Figure 1.** SEM images of cobalt nanowires grown under the following conditions: 5 kV, 86 pA
4 and working pressure (minus base pressure) of (a) 7.3×10^{-6} mbar, (b) 6.4×10^{-6} mbar, (c) $5.9 \times$
5 10^{-6} mbar, and (d) 5.1×10^{-6} mbar. The transition from linear to radial growth mode with
6 decreasing precursor flux is noticed.
7
8
9

10
11
12
13
14 Similarly to the case of in-plane deposits, the height growth rate of the obtained nanowires
15 increases with the working pressure, as shown in Figure 2, which is indicative of growth in the
16 precursor-limited regime [44]. However, as noticed in this figure, a change in the growth-rate slope
17 is observed at the crossover between the linear and radial growth modes, highlighted with two
18 visual guide lines. It should be stressed that the average height growth rate is well defined for
19 nanowires with pure linear or radial growth modes but, in the case of nanowires with transition
20 between both modes, this value will depend on the relative contribution of both segments to the
21 total height. The height growth rate was determined from data in Table 1 considering the total
22 height of the nanowire and the deposition time, defined as the time spent to grow it. Additionally,
23 the volume growth rate as a function of the working pressure was calculated, increasing linearly
24 in the linear growth mode.
25
26
27
28
29
30
31
32
33
34
35
36
37
38
39
40
41
42
43
44
45
46
47
48
49
50
51
52
53
54
55
56
57
58
59
60

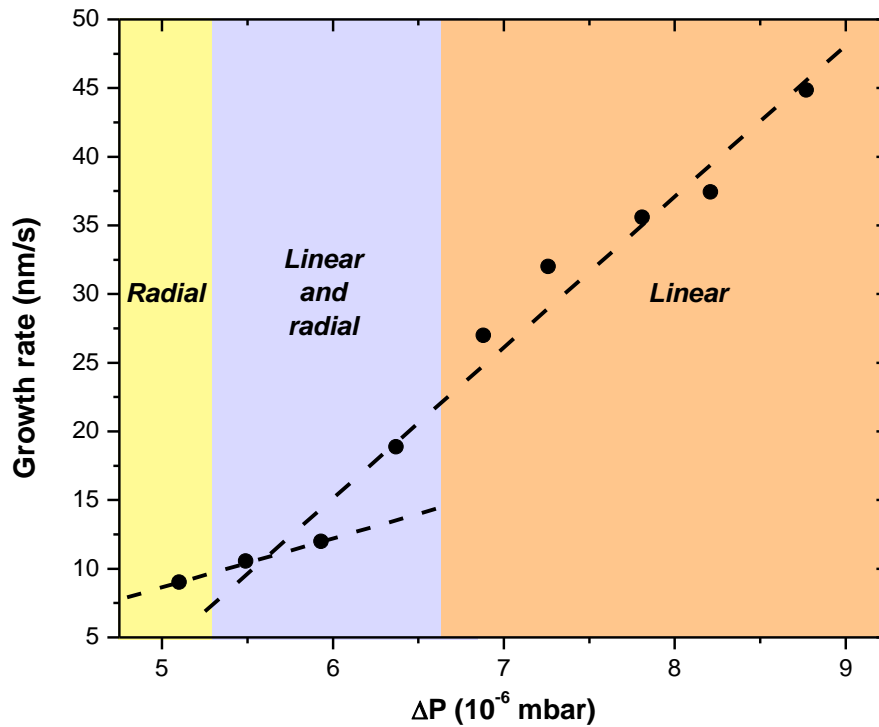


Figure 2. Growth rate of nanowires grown at 5 kV and 86 pA as a function of the working pressure (minus base pressure). A change in slope is noticed at the crossover from radial to linear growth modes. In the “linear and radial” growth mode, the nanowire presents two segments, one with the features of the linear mode and one with the features of the radial mode.

Table 1. Data of the nanowires represented in Figure 2: height, deposition time, growth rate and working pressure (minus base pressure) during growth.

Height (μm)	Deposition time (s)	Growth rate (nm/s)	ΔP (10^{-6} mbar)
1.66	37	44.9	8.8
1.61	43	37.4	8.2
1.53	43	35.6	7.8

1.60	50	32.0	7.3
1.35	50	27.0	6.9
0.944	50	18.9	6.4
0.599	50	12.0	5.9
0.655	62	10.6	5.5
0.614	68	9.0	5.1

As shown in Figure 3, the composition of the deposits is strongly affected by the precursor flux. A dedicated experiment was performed in which the electron beam current was fixed to 100 pA. At that beam current, the crossover from the radial-growth regime to the linear-growth regime occurs at ΔP of 1.75×10^{-5} mbar. Overall, the behavior of the Co content as a function of working pressure resembles that observed in in-plane deposits [38]: an optimum precursor flux window (1×10^{-5} mbar $< \Delta P < 1.5 \times 10^{-5}$ mbar) exists where the Co content is high ($\sim 85\%$). Although specific experiments and/or simulations could shed more light on the origin of this change in composition, from general arguments it can be stated that at lower precursor flux the Co content can diminish due to decomposition of residual contaminant species in the chamber, whereas at higher precursor flux the Co content can diminish due to incomplete precursor decomposition. The different origin of the decreased Co content at low and high precursor flux can be also noted in the C/O ratio, which is smaller than 1 at high precursor flux and larger than 1 at low precursor flux (see Figure 3). From Figure 3, it is clear that optimum Co content ($> 85\%$) can be only achieved in the radial-growth mode, where the diameter is at least ≈ 120 nm.

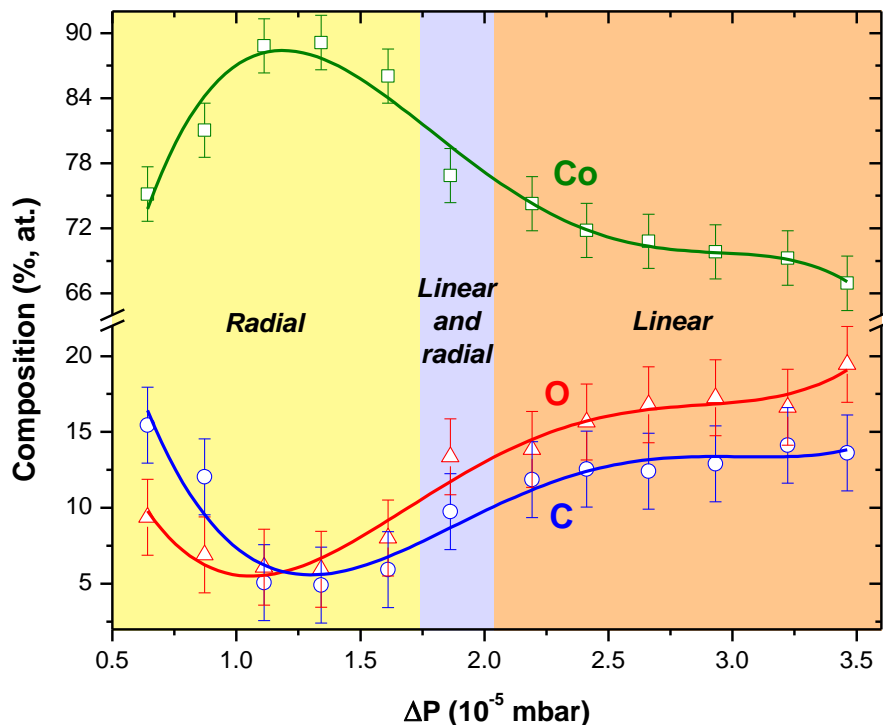


Figure 3. Composition of NWs grown using 5 kV and 100 pA as a function of the working pressure (minus base pressure). EDS measurements were performed at 5 kV and 800 pA. Three different growth regimes can be noticed. The composition of the sample falling in the “linear and radial” regime has been determined at the base of the nanowire, which corresponds to the linear-growth mode.

In order to correlate the Co content of the nanowires with their magnetization, dedicated experiments have been carried out inside the TEM. The experiment consists of EDS of all nanowires and EELS of two selected nanowires. EH has also been performed on selected individual nanowires to obtain quantitative values of the Co content and the magnetic induction inside the nanowire. In Figure 4, the Co content is represented as a function of the nanowire’s

diameter for optimum growth conditions. The specific growth parameters of each nanowire displayed in Figure 4 are described in Table 2. Figure 4 indicates that a high Co content ($> 85\%$) can be achieved in nanowires with diameter larger than ≈ 120 nm, which correspond to the radial-growth mode. However, the Co content in nanowires with diameter smaller than ≈ 80 nm, which correspond to the linear-growth mode, is around 80% for diameters of ≈ 80 nm, but diminishes quickly as the diameter is reduced. For diameters of ≈ 60 nm, the Co content is only $\sim 45\%$. Given that the nanowires present typical oxidized shells of around 5 nm [41], the measured average Co content will be lower as the wire diameter decreases. This means that in the core of the nanowire the Co content is expected to be higher than the average value, this effect being more significant for the narrowest wires.

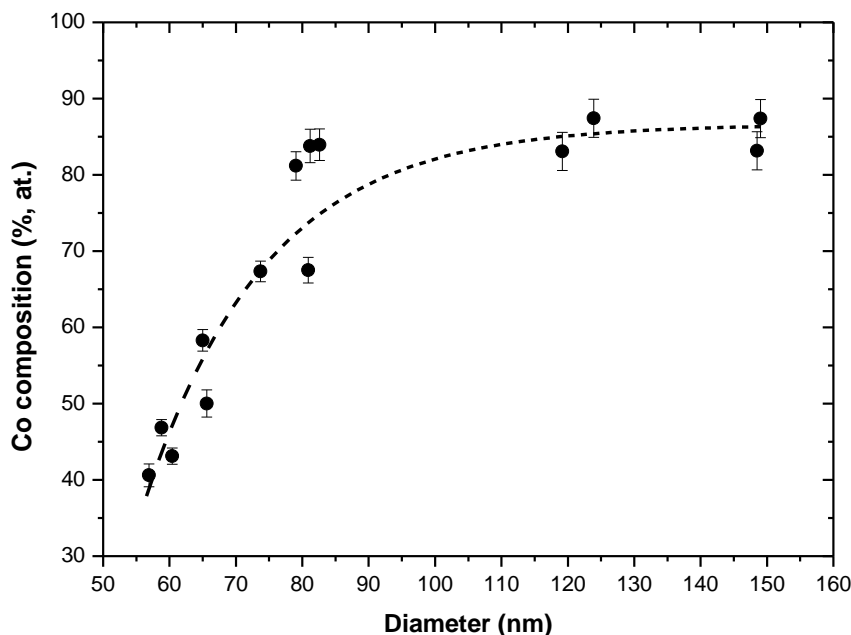


Figure 4. Cobalt composition as a function of the wire diameter for optimized growth conditions at each particular value of the diameter.

Table 2. Data of the nanowires represented in Figure 4: diameter, Co content and technique used for its measurement, beam current and working pressure (minus base pressure) during growth. The beam energy used for the growth was 5 kV.

Diameter (nm)	Co composition (% , at.)	Technique	Growth current (pA)	ΔP (10^{-6} mbar)
56.9	40.6	EDS	50	2.8
58.8	46.9	EDS	25	10.3
60.4	43.1	EDS	50	10.2
65.0	58.3	EDS	100	10.5
65.6	50.0	EDS	100	9.3
73.7	67.3	EDS	100	8.1
79.1	81.2	EDS	50	6.9
80.9	67.5	EDS	100	8.1
81.2	83.8	EDS	100	8.4
82.6	84.0	EDS	50	7.8
119.2	83.1	EELS	50	2.8
123.9	87.4	EDS	50	5.2
148.5	83.2	EDS	100	6.9
149.0	87.4	EELS	100	6.1

The magnetic induction of selected nanowires has been investigated by means of EH. Each nanowire is measured in magnetic remanence after previously saturating the magnetization in two opposite directions by applying an external magnetic field produced by the objective lens. This is a common method to get rid of the electrostatic contribution to the phase change and to reveal the magnetic contribution after subtraction of both measurements. Following the electron holography method described in previous work [41], the average magnetic induction inside a nanowire along its long axis, B_x , can be calculated as:

$$|B_x(x,y)| = \frac{\hbar}{e \cdot t} \frac{\partial \varphi_{MAG}(x,y)}{\partial y} \quad (1)$$

where \hbar is the reduced Planck constant, φ_{MAG} the magnetic component of the total electron phase shift $\varphi(\vec{r})$, e the electron charge and t the variable thickness along the specimen width. In Figure 5, the results corresponding to three nanowires, representative of the three regimes found in this study, are shown. The values obtained for B_x close to the nanowire borders are not reliable due to the uncertainties in the sample thickness at those positions and edge effects at the oxidized wire surface. For this reason, in Figure 5 the values of B_x obtained at the edges of the nanowires are masked with a semi-transparent band. However, the values obtained in the central part of the nanowires are trustworthy. The nanowire with the largest diameter, 123.9 nm, corresponding to the radial-growth mode, presents a high magnetic induction along the long wire axis of ~ 1.33 T, not far from the bulk value, 1.8 T. This high value of the magnetization correlates well with the high Co content in the nanowire, 87.4%. A second nanowire, corresponding to the intermediate linear-radial-growth mode has been analyzed by EH at the base, in the portion with linear-growth mode. It presents a magnetic induction along the long wire axis of 0.78 T, around 50% of the bulk magnetization of Co. This reduction is expected given the reduced Co content (67.5%) in this nanowire. A third nanowire, corresponding to the linear-growth mode, presents a lower magnetic induction along the long wire axis of 0.41 T, which can be expected given its reduced Co content (40.6%). However, we would like to point out that the obtained magnetic induction in the nanowires is sufficiently high for functional nanomagnetic devices and applications. Just as an example, the Fe magnetic rods used in the past by Franken et al. had magnetization of 0.13 T along their long axis and were able to pin domain walls in a domain-wall conduit [16].

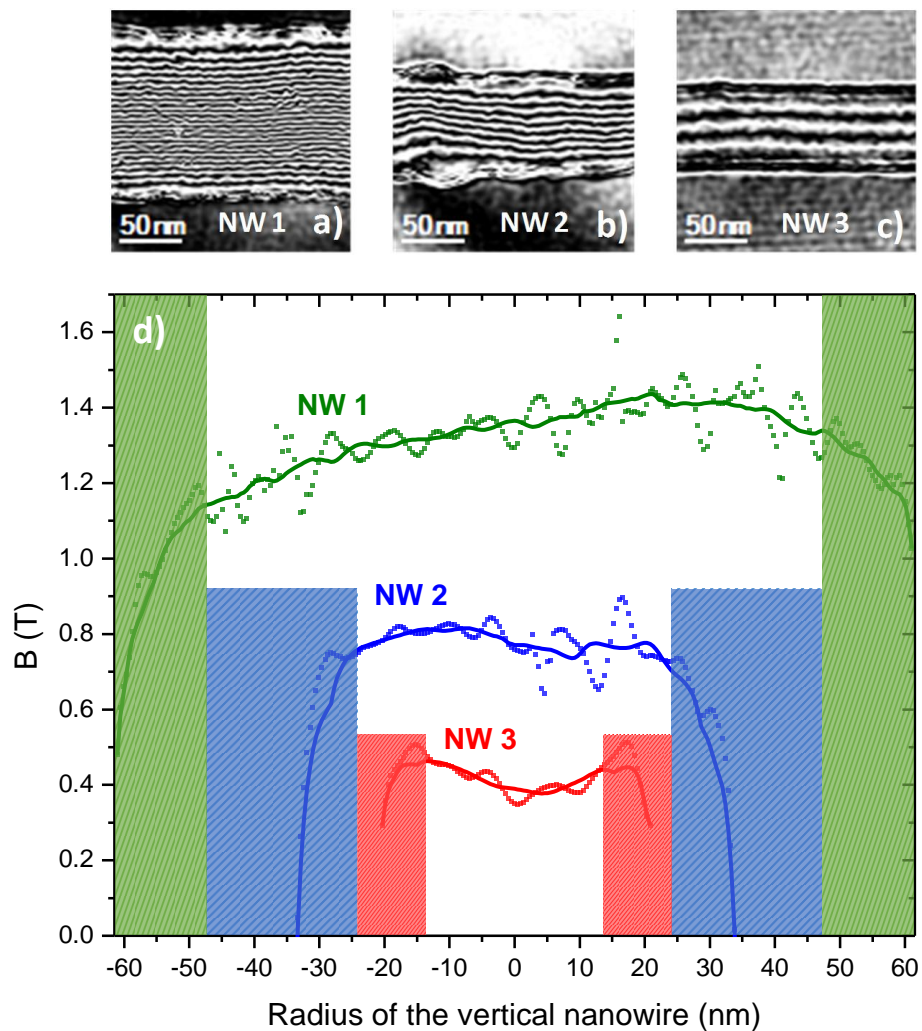


Figure 5. a) Representation of the magnetic induction flux of a nanowire with cobalt content of 87.4% at. (NW1), obtained from the magnetic phase images after normalizing by the maximum thickness and performing the cosine of 700 times the change in electron phase; b) the same for the nanowire with cobalt content of 67.5% at. (NW2); c) the same for the nanowire with cobalt content of 40.6% at. (NW3); d) profiles of the magnetic induction along the short axis of nanowires NW1, NW2 and NW3, obtained from the magnetic phase images used to calculate a), b) and c), respectively. The edges of the nanowires are partially masked given that quantification is not reliable due to edge effects.

4. Discussion

FEBID growth of functional magnetic nanostructures requires precise control of a high number of growth parameters. Their precise tuning can be crucial in particular cases, such as the growth of Co three-dimensional nanowires discussed in the present work. In the process of optimization of their growth, we have encountered a number of interesting phenomena that should be taken into account for their practical application. The first important finding regards the existence of two growth modes with different physical properties, denoted linear and radial due to certain similarities with reported growth of three-dimensional iron nanowires [45]. In the radial-growth mode, the minimum diameter obtained is ≈ 120 nm and the Co content can be very high, $> 85\%$, showing a high magnetization, not far from the bulk value, 1.8 T. In the linear-growth mode, the diameter can be lower than ≈ 80 nm and the Co content diminishes for decreasing diameter. For a diameter of 80 nm, nanowires can attain Co content of 80% and show magnetization around half the bulk value. However, if the diameter is 60 nm, the Co content is found to be 45% and the magnetization is around 1/4 of the bulk value. We cannot discard that the nanowires of low Co content have areas with inhomogeneous composition, the areas richer in Co contributing more to the magnetization of the nanowire. Interestingly, inside the same nanowire, a transition between both growth modes can be observed in a certain range of growth parameters. This effect seems to indicate that thermal desorption and decreased diffusion effects during the growth of high-aspect-ratio 3D nanostructures may be playing a key role. The capacity to dissipate the heat caused by the electron beam is reduced as the nanowire grows, being the tip growing progressively further away from the substrate. At a certain height, there is an overheating which could result in a change of the growth mode. The existence of single nanowires with two diameters seems useful for studies

1
2
3 of magnetic-domain-wall propagation in nanowires, given their tendency to become pinned at the
4 location of the transition between both diameters [51].
5
6
7

8
9 The correlation found between the diameter of the nanowire and its composition is important
10 given the relationship observed between the Co content and the magnetization of the nanowire. If
11 a nanowire with magnetization close to the bulk value, 1.8 T, is required, the best option is to grow
12 a nanowire with diameter of at least 120 nm. However, in many practical situations, narrow
13 nanowires (< 100 nm) are required, in which case, a maximum Co content of $\sim 80\%$ can be
14 achieved, this value diminishing strongly with decreasing diameter. In such situation, the
15 magnetization is observed to decrease with respect to the bulk value despite being still quite large
16 in absolute value. There are a few potential applications of these nanowires such as magnetic
17 functionalization of cantilevers [52] [11] [17] [53] [13], three-dimensional logic structures [17]
18 [39], cylindrical conduits for domain-wall propagation [14], superconducting vortex lattice
19 pinning [40] [54], remote magnetomechanical actuation [20], etc. where lateral resolution is more
20 important than the absolute value of the magnetization. In those cases, the type of nanowires grown
21 here in the linear-growth mode meet the required physical properties. Another strategy to enhance
22 the Co content is to perform post-annealing treatments [55] [56]. It has been shown that in-plane
23 Co structures can be purified by annealing in vacuum conditions, eliminating the oxygen content
24 of the deposits [56]. This could be a viable strategy to obtain narrow Co nanowires (< 100 nm in
25 diameter) with very high Co content ($> 90\%$) and the associated magnetization close to the bulk
26 value.
27
28
29
30
31
32
33
34
35
36
37
38
39
40
41
42
43
44
45
46
47
48
49
50
51
52
53
54
55

56 **5. Conclusions**

57
58
59
60

1
2
3 To conclude, we have shown that control of the growth parameters in focused-electron-beam-
4 induced deposition, especially the electron beam current and the precursor flux, allows tuning the
5 diameter, composition and magnetization of three-dimensional cobalt nanowires, grown using the
6 $\text{Co}_2(\text{CO})_8$ precursor. A transition between two growth modes, radial and linear, has been unveiled
7 in single nanowires, resulting in individual nanowires with two different diameters (80 nm and
8 120 nm respectively). The best growth conditions to achieve nanowires with small diameter
9 (< 80 nm), high metallic content (~80%) and high magnetization (~0.9 T) have been identified,
10 providing a growth route for various applications.
11
12
13
14
15
16
17
18
19
20
21
22
23
24
25

26 **Acknowledgment**

27
28
29
30 This work was supported by Spanish Ministry of Economy and Competitivity through projects
31 No. MAT2014-51982C2-1-R, MAT2014-51982C2-2-R and MAT2015-69725-REDT, including
32 FEDER funds and by the Aragon Regional Government (Construyendo Europa desde Aragón)
33 through project E26, with FEDER funding. This work was conducted within the framework of the
34 COST Action CM1301 (CELINA). AFP acknowledges funding from a EPSRC Early Career
35 Fellowship EP/M008517/1 and from a Winton Fellowship. J. P.-N. grant is funded by the *Ayuda*
36 *para Contratos Predoctorales para la Formación de Doctores, Convocatoria Res. 05/06/15* (BOE
37 12/06/15) of the *Secretaría de Estado de Investigación, Desarrollo e Innovación* in the
38 *Subprograma Estatal de Formación* of the Spanish Ministry of Economy and Competitiveness
39 (MINECO) with the participation of the European Social Fund. Experimental help clean-room
40 technicians from “Laboratorio de Microscopías Avanzadas” (LMA) are warmly acknowledged.
41
42
43
44
45
46
47
48
49
50
51
52
53
54
55
56
57
58
59
60

1
2
3 Discussions with Dr. Luis Serrano-Ramón about the growth conditions and the nature of the linear
4
5 and radial growth modes are acknowledged.
6
7
8
9
10

11 12 **References**

- 13
14
15
16 [1] Hartmann U 2000 *Magnetic multilayers and giant magnetoresistance: fundamentals and*
17 *industrial applications* (Springer)
18
19
20
21 [2] Fert A 2008 Origin, development, and future of spintronics (Nobel lecture) *Rev. Mod. Phys.*
22 **80** 1517–30
23
24
25
26
27 [3] Candini a, Gazzadi G C, Bona a Di, Affronte M, Ercolani D, Biasiol G and Sorba L 2006
28 Hall nano-probes fabricated by focused ion beam *Nanotechnology* **17** 2105–9
29
30
31
32
33 [4] Chappert C, Fert A and Van Dau F N 2007 The emergence of spin electronics in data
34 storage. *Nat. Mater.* **6** 813–23
35
36
37
38
39 [5] Niemier M T, Bernstein G H, Csaba G, Dingler A, Hu X S, Kurtz S, Liu S, Nahas J, Porod
40 W, Siddiq M and Varga E 2011 Nanomagnet logic: progress toward system-level
41 integration *J. Phys. Condens. Matter* **23** 493202
42
43
44
45
46
47 [6] Castagné M, Benfedda M, Lahimer S, Falgayrettes P and Fillard J P 1999 Near field optical
48 behaviour of C supertips *Ultramicroscopy* **76** 187–94
49
50
51
52
53 [7] Gazzadi G C, Frabboni S and Menozzi C 2007 Suspended nanostructures grown by electron
54 beam-induced deposition of Pt and TEOS precursors *Nanotechnology* **18** 445709
55
56
57
58
59
60

- 1
2
3 [8] Bøggild P, Hansen T M, Tanasa C and Grey F 2001 Fabrication and actuation of
4 customized nanotweezers with a 25 nm gap *Nanotechnology* **12** 331–5
5
6
7
8
9 [9] Höflich K, Yang R Bin, Berger A, Leuchs G and Christiansen S 2011 The Direct Writing
10 of Plasmonic Gold Nanostructures by Electron-Beam-Induced Deposition *Adv. Mater.* **23**
11 2657–61
12
13
14
15
16
17 [10] Fowlkes J D, Winkler R, Lewis B B, Stanford M G, Plank H and Rack P D 2016
18 Simulation-Guided 3D Nanomanufacturing via Focused Electron Beam Induced Deposition
19 *ACS Nano* **10** 6163–72
20
21
22
23
24
25 [11] Utke I, Hoffmann P, Berger R and Scandella L 2002 High-resolution magnetic Co supertips
26 grown by a focused electron beam *Appl. Phys. Lett.* **80** 4792–4
27
28
29
30
31 [12] Takeguchi M, Shimojo M, Che R and Furuya K 2006 Fabrication of a nano-magnet on a
32 piezo-driven tip in a TEM sample holder *J. Mater. Sci.* **41** 2627–30
33
34
35
36
37 [13] Belova L M, Hellwig O, Dobisz E and Dan Dahlberg E 2012 Rapid preparation of electron
38 beam induced deposition Co magnetic force microscopy tips with 10 nm spatial resolution
39 *Rev. Sci. Instrum.* **83**
40
41
42
43
44
45 [14] Fernández-Pacheco A, Serrano-Ramón L, Michalik J M, Ibarra M R, De Teresa J M,
46 O’Brien L, Petit D, Lee J and Cowburn R P 2013 Three dimensional magnetic nanowires
47 grown by focused electron-beam induced deposition. *Sci. Rep.* **3** 1492
48
49
50
51
52
53 [15] Lavenant H 2014 Mechanical magnetometry of Cobalt nanospheres deposited by focused
54 electron beam at the tip of ultra-soft cantilevers *Nanofabrication* **1** 65–73
55
56
57
58
59
60

- 1
2
3 [16] Franken J H, Van Der Heijden M A J, Ellis T H, Lavrijsen R, Daniels C, McGrouther D,
4 Swagten H J M and Koopmans B 2014 Beam-induced Fe nanopillars as tunable domain-
5 wall pinning sites *Adv. Funct. Mater.* **24** 3508–14
6
7
8
9
10
11 [17] Gavagnin M, Wanzenboeck H D, Wachter S, Shawrav M M, Persson A, Gunnarsson K,
12 Svedlindh P, Stöger-Pollach M and Bertagnolli E 2014 Free-standing magnetic nanopillars
13 for 3D nanomagnet logic *ACS Appl. Mater. Interfaces* **6** 20254–60
14
15
16
17
18
19 [18] Gazzadi G C and Frabboni S 2015 Structural transitions in electron beam deposited Co-
20 carbonyl suspended nanowires at high electrical current densities. *Beilstein J. Nanotechnol.*
21 **6** 1298–305
22
23
24
25
26
27 [19] Perez-Roldan M J, Tatti F, Vavassori P, Berger a and Chuvilin a 2015 Segregation of
28 materials in double precursor electron-beam-induced-deposition: a route to functional
29 magnetic nanostructures *Nanotechnology* **26** 375302
30
31
32
33
34
35 [20] Vavassori P, Pancaldi M, Perez-Roldan M J, Chuvilin A and Berger A 2016 Remote
36 Magnetomechanical Nanoactuation *Small* 1–11
37
38
39
40
41 [21] Randolph S J, Fowlkes J D and Rack P D 2006 Focused, Nanoscale Electron-Beam-
42 Induced Deposition and Etching *Crit. Rev. Solid State Mater. Sci.* **31** 55–89
43
44
45
46
47 [22] Van Dorp W F and Hagen C W 2008 A critical literature review of focused electron beam
48 induced deposition *J. Appl. Phys.* **104** 81301
49
50
51
52
53 [23] Utke I, Hoffmann P and Melngailis J 2008 Gas-Assisted Focused Electron Beam and Ion
54 Beam Processing and Fabrication *J. Vac. Sci. Technol. B Microelectron. Nanom. Struct.* **26**
55
56
57
58
59
60

- 1
2
3 1197–276
4
5
6
7 [24] Huth M, Porrati F, Schwalb C, Winhold M, Sachser R, Dukic M, Adams J and Fantner G
8
9 2012 Focused electron beam induced deposition: A perspective *Beilstein J. Nanotechnol.* **3**
10
11 597–619
12
13
14
15 [25] Plank H, Smith D A, Haber T, Rack P D and Hofer F 2012 Fundamental proximity effects
16
17 in focused electron beam induced deposition *ACS Nano* **6** 286–94
18
19
20
21 [26] Winkler R, Szkudlarek A, Fowlkes J D, Rack P D, Utke I and Plank H 2015 Toward
22
23 ultraflat surface morphologies during focused electron beam induced nanosynthesis:
24
25 Disruption origins and compensation *ACS Appl. Mater. Interfaces* **7** 3289–97
26
27
28
29 [27] Fernández-Pacheco a, De Teresa J M, Córdoba R and Ibarra M R 2009 Magnetotransport
30
31 properties of high-quality cobalt nanowires grown by focused-electron-beam-induced
32
33 deposition *J. Phys. D. Appl. Phys.* **42** 55005
34
35
36
37 [28] Takeguchi M, Shimojo M and Furuya K 2005 Fabrication of magnetic nanostructures using
38
39 electron beam induced chemical vapour deposition *Nanotechnology* **16** 1321–5
40
41
42
43 [29] Lavrijsen R, Córdoba R, Schoenaker F J, Ellis T H, Barcones B, Kohlhepp J T, Swagten H
44
45 J M, Koopmans B, De Teresa J M, Magén C, Ibarra M R, Trompenaars P and Mulders J J
46
47 L 2011 Fe:O:C grown by focused-electron-beam-induced deposition: magnetic and electric
48
49 properties *Nanotechnology* **22** 25302
50
51
52
53 [30] Perentes A, Sinicco G, Boero G, Dwir B and Hoffmann P 2007 Focused electron beam
54
55 induced deposition of nickel *J. Vac. Sci. Technol. B Microelectron. Nanom. Struct.* **25** 2228
56
57
58
59
60

- 1
2
3 [31] Córdoba R, Barcones B, Roelfsema E, Verheijen M A, Mulders J J L, Trompenaars P H F
4 and Koopmans B 2016 Functional nickel-based deposits synthesized by focused beam
5 induced processing *Nanotechnology* **27** 65303
6
7
8
9
10
11 [32] Nikulina E, Idigoras O, Porro J M, Vavassori P, Chuvilin A and Berger A 2013 Origin and
12 control of magnetic exchange coupling in between focused electron beam deposited cobalt
13 nanostructures *Appl. Phys. Lett.* **103** 123112
14
15
16
17
18
19 [33] Gavagnin M, Wanzenboeck H D, Belic D, Shawrav M M, Persson A, Gunnarsson K,
20 Svedlindh P and Bertagnolli E 2014 Magnetic force microscopy study of shape engineered
21 FEBID iron nanostructures *Phys. Status Solidi Appl. Mater. Sci.* **211** 368–74
22
23
24
25
26
27 [34] De Teresa J M and Fernández-Pacheco A 2014 Present and future applications of magnetic
28 nanostructures grown by FEBID *Appl. Phys. A* **117** 1645–58
29
30
31
32
33 [35] De Teresa J M, Fernández-Pacheco A, Córdoba R, Serrano-Ramón L, Sangiao S and Ibarra
34 M R 2016 Review of magnetic nanostructures grown by focused electron beam induced
35 deposition (FEBID) *J. Phys. D Appl. Phys. Phys.* **49** 243003
36
37
38
39
40
41 [36] Guo F, Belova L M and McMichael R D 2013 Spectroscopy and imaging of edge modes
42 in permalloy nanodisks *Phys. Rev. Lett.* **110** 1–5
43
44
45
46
47 [37] Gabureac M, Bernau L, Utke I and Boero G 2010 Granular Co–C nano-Hall sensors by
48 focused-beam-induced deposition *Nanotechnology* **21** 115503
49
50
51
52
53 [38] Serrano-Ramón L, Córdoba R, Rodríguez L A, Magén C, Snoeck E, Gatel C, Serrano I,
54 Ibarra M R and De Teresa J M 2011 Ultrasmall functional ferromagnetic nanostructures
55
56
57
58
59
60

- 1
2
3 grown by focused electron-beam-induced deposition *ACS Nano* **5** 7781–7
4
5
6
7 [39] Sharma N, Mourik R A van, Yin Y, Koopmans B and Parkin S S P 2016 Focused-electron-
8
9 beam-induced-deposited cobalt nanopillars for nanomagnetic logic *Nanotechnology* **27**
10
11 165301
12
13
14 [40] Dobrovolskiy O V., Begun E, Huth M, Shklovskij V A and Tsindlekht M I 2011 Vortex
15
16 lattice matching effects in a washboard pinning potential induced by Co nanostripe arrays
17
18 *Phys. C Supercond. its Appl.* **471** 449–52
19
20
21
22
23 [41] Pablo-Navarro J, Magén C and de Teresa J M 2016 Three-dimensional core-shell
24
25 ferromagnetic nanowires grown by focused electron beam induced deposition
26
27 *Nanotechnology* **27** 285302
28
29
30
31 [42] Belić D, Shawrav M M, Gavagnin M, Stöger-Pollach M, Wanzenboeck H D and
32
33 Bertagnolli E 2015 Direct-write deposition and focused-electron-beam-induced purification
34
35 of gold nanostructures *ACS Appl. Mater. Interfaces* **7** 2467–79
36
37
38
39 [43] Córdoba R, Sharma N, Kölling S, Koenraad P M and Koopmans B 2016 High-purity 3D
40
41 nano-objects grown by focused-electron-beam induced deposition. *Nanotechnology* **27**
42
43 355301
44
45
46
47 [44] Wachter S, Gavagnin M, Wanzenboeck H D, Shawrav M M, Belić D and Bertagnolli E
48
49 2014 Nitrogen as a carrier gas for regime control in focused electron beam induced
50
51 deposition *Nanofabrication* **1** 16–22
52
53
54
55 [45] Hochleitner G, Wanzenboeck H D and Bertagnolli E 2008 Electron beam induced
56
57
58
59
60

- 1
2
3 deposition of iron nanostructures *J. Vac. Sci. Technol. B Microelectron. Nanom. Struct.* **26**
4
5 939
6
7
8
9 [46] Córdoba R, Sesé J, De Teresa J M and Ibarra M R 2010 High-purity cobalt nanostructures
10 grown by focused-electron-beam-induced deposition at low current *Microelectron. Eng.* **87**
11 1550–3
12
13
14
15
16
17 [47] Belova L M, Dahlberg E D, Riazanova a, Mulders J J L, Christophersen C and Eckert J
18 2011 Rapid electron beam assisted patterning of pure cobalt at elevated temperatures via
19 seeded growth. *Nanotechnology* **22** 145305
20
21
22
23
24
25 [48] Van Dorp W F, Hansen T W, Wagner J B and De Hosson J T M 2013 The role of electron-
26 stimulated desorption in focused electron beam induced deposition *Beilstein J.*
27 *Nanotechnol.* **4** 474–80
28
29
30
31
32
33 [49] Serrano-Esparza I, Córdoba R, Mulders J J L, Ibarra M R and Teresa J M De 2015 Precursor
34 competition in focused-ion-beam-induced co-deposition from W(CO)₆ and C₁₀H₈
35 *ScienceJet* **4** 1–9
36
37
38
39
40
41 [50] Szkudlarek A, Gabureac M and Utke I 2011 Determination of the Surface Diffusion
42 Coefficient and the Residence Time of Adsorbates via Local Focused Electron Beam
43 Induced Chemical Vapour Deposition *J. Nanosci. Nanotechnol.* **11** 8074–8
44
45
46
47
48
49 [51] Berganza E, Bran C, Jaafar M, Vázquez M and Asenjo A 2016 Domain wall pinning in
50 FeCoCu bamboo-like nanowires *Sci. Rep.* **6** 29702
51
52
53
54
55 [52] Lau Y M, Chee P C, Thong J T L and Ng V 2002 Properties and applications of cobalt-
56
57
58
59
60

1
2
3 based material produced by electron-beam-induced deposition *J. Vac. Sci. Technol. A*
4
5
6 *Vacuum, Surfaces, Film.* **20** 1295
7

8
9 [53] Tosolini G, Michalik J M, Córdoba R, de Teresa J M, Pérez-Murano F and Bausells J 2014
10
11 Magnetic properties of cobalt microwires measured by piezoresistive cantilever
12
13 magnetometry *Nanofabrication* **1** 80–5
14
15

16
17 [54] Dobrovolskiy O V, Huth M and Shklovskij V a 2010 Anisotropic magnetoresistive
18
19 response in thin Nb films decorated by an array of Co stripes *Supercond. Sci. Technol.* **23**
20
21 125014
22
23

24
25 [55] Begun E, Dobrovolskiy O V, Kompaniets M, Sachser R, Gspan C, Plank H and Huth M
26
27 2015 Post-growth purification of Co nanostructures prepared by focused electron beam
28
29 induced deposition *Nanotechnology* **26** 75301
30
31

32
33 [56] Puydinger dos Santos M V., Velo M F, Domingos R D, Zhang Y, Maeder X, Guerra-Nuñez
34
35 C, Best J P, Béron F, Pirota K R, Moshkalev S, Diniz J A and Utke I 2016 Annealing-Based
36
37 Electrical Tuning of Cobalt–Carbon Deposits Grown by Focused-Electron-Beam-Induced
38
39 Deposition *ACS Appl. Mater. Interfaces* acsami.6b12192
40
41
42
43
44
45
46
47
48
49
50
51
52
53
54
55
56
57
58
59
60